Computational Assessment of Alkali-Silica-Reaction Impact on the Seismic Capacity of Nuclear Containment Vessels

Albert Dahal[a], Benjamin W. Spencer[b,*], Somayajulu L. N. Dhulipala[b], Amit Jain[b], Luis F. Ibarra[a]

[a] *University of Utah, 201 Presidents' Cir., Salt Lake City, UT 84112*
[b] *Idaho National Laboratory, P.O. Box 1625, Idaho Falls, ID 83415-3840*

Abstract

This study assesses the effects of alkali-silica reaction (ASR) on the seismic performance of containment vessels (CVs), which serve as a final barrier against radioactive contaminant release from light-water nuclear reactors during a severe accident. ASR is an aging degradation mechanism that affects a variety of reinforced concrete structures and has been observed in multiple operating nuclear plants. This study simulates ASR progression and its effects on a reinforced concrete CV, employing a fully coupled multiphysics model that accounts for the interaction between thermal and moisture transport and the mechanical stress states. The ASR's effects on the seismic response of the CV after long-term environmental exposure was simulated using a unified modeling approach. The structure's seismic performance was evaluated using incremental dynamic analysis (IDA) for a suite of ground motion records applied to pristine and degraded vessels. Fragility functions were developed for functional and collapse limit states to study the ability of the structure to maintain leak tightness and structural integrity, respectively. High-performance computing enabled completing the large set of seismic analyses required for the IDA. The results show a higher probability of exceeding the functional limit state with the ASR-degraded vessel, which potentially indicates an increased risk of contaminant release due to ASR. ASR degradation has a minimal impact on the median collapse capacity of the CV, but does increase the uncertainty in the collapse capacity.

Keywords: Alkali-silica reaction, Containment vessel, Multiphysics simulation, Seismic fragility

1. Introduction

Containment vessels (CVs) are employed in light-water nuclear reactors to act as the final barrier against the release of fission products in the unlikely event of a breach of the primary coolant system. The CV must maintain its structural integrity under a variety of conditions, including natural hazards such as earthquakes. Containment vessel designs vary considerably, and they can be constructed of steel, reinforced concrete (RC), or prestressed concrete. Concrete CVs are exposed to environmental conditions and thus are subject to age-related concrete degradation. Nuclear power plant (NPP) structures are unique in that they potentially experience chronic degradation due to irradiation. Because CVs are protected from radiation from the reactor by a concrete biological shield wall, their exposure to radiation is minimal [1]. However, other environmental degradation mechanisms such as corrosion and alkali-silica reaction (ASR)

*Corresponding author
Email address: `benjamin.spencer@inl.gov` (Benjamin W. Spencer)

are also potential causes for concern [2, 1]. ASR is a chemical process involving interactions between alkali ions, silica present in the aggregates, and moisture within the concrete matrix. The alkali ions diffuse into the porous aggregates, leading to the dissolution of silica components and the formation of hydrophilic silica gel. This silica gel expands in the presence of moisture and, over time, exerts internal pressure on the concrete matrix, causing microcracks [3]. ASR-induced degradation has been documented in operational NPPs. Notably, ASR-driven damage was identified at the Seabrook NPP in 2009 [4], and ASR-induced expansion was observed in 1979 at the Ikata NPP [5]. In the latter case, the expansion, which was attributed to silicate minerals in the coarse aggregate, impacted the generator's functionality and required equipment adjustments. While such functional impacts of concrete degradation are important, the detrimental impact of concrete degradation on structural capacity during extreme loading events is potentially of greater concern. Given the need to extend the operational lives of aging power reactors—and the requisite operating license renewals that go along with this—it is crucial to accurately evaluate the impact of degradation mechanisms such as ASR on the CV's structural capacity, especially under natural hazards such as earthquakes.

RC CVs differ from other civil RC structures in scale, design, and functionality. The stringent design and safety requirements [6, 7] of RC CVs enable them to withstand elevated internal pressure or external loads due to natural hazards. Experimental studies assessing the structural capacity of containment structures are relatively scarce due to the extreme difficulty of performing such tests. These studies mainly involve overpressurization [8, 9] or shake-table loading [10, 11] of scaled-down CV models. Although these scaled-down tests offered important insight into the expected behavior of specific types of CVs, the effects of material degradation were not considered. Due to the complexity of physical model testing, seismic capacity assessment of CVs is often performed using finite element (FE) analysis. To this end, researchers have used fragility analysis with finite element models as an effective safety assessment tool. This type of analysis fits into the broader seismic probabilistic risk assessment framework used in the nuclear industry.

Either simplified lumped-mass models [12, 13, 14] or three-dimensional (3D) FE models [15] can be used for the structural modeling of CVs. Lumped-mass models simplify the containment geometry as a series of masses connected by beams and are computationally inexpensive. However, this approach is inadequate for studying the local distribution of stresses and strains, particularly in the nonlinear regime. The lumped-mass approach has been used to assess the seismic fragility of NPPs considering recorded earthquakes in Korea [12]. Likewise, seismic fragility analyses of the CANDU (Canadian Natural-Uranium, Heavy-Water-moderated-and-Cooled) power reactor [13] and Indian pressurized heavy water reactor containment [14] were performed with a lumped-mass approach. The latter used two-dimensional fiber sections in the OpenSees code and proposed a novel fragility analysis method using incremental dynamic analysis (IDA).

Three-dimensional FE models capture the complex interactions and detailed stress distributions within the containment structure. These models can simulate critical 3D stress states, local effects, and nonlinear material behavior, which are essential for understanding CV response during seismic events. Numerous recent studies of CV integrity have employed 3D computational modeling approaches. For example, the influence of vertical ground motion (GM) on horizontal response and the seismic fragility of the containment considering basemat uplift was evaluated by Nakamura et al. [15, 16] using this approach. Jin and Gong [17] and Jin et al. [18] assessed the probabilistic seismic performance of existing containment structures under near-fault and far-fault earthquakes and developed seismic fragility curves. These studies found the lower part of the vessel to be more susceptible to seismic-induced damages. Bao et al. [19] and Bao et al. [20] studied the seismic response of a CV subjected to a mainshock-aftershock sequence considering the damage induced in the CV by the mainshock. Jin et al. [21] performed a probabilistic failure analysis of a CV under internal pressurization following a seismic event and found that the pressure capacity of the vessel decreases with increasing earthquake intensity. Lin et al. [22] performed a computational failure analysis of a CV under several earthquakes and presented a range of seismic intensity levels at which the failure limit states (LSs) were exceeded. They also performed a safety assessment of the CV under a representative earthquake and subsequent tsunami event, considering variable inundation depths.

These seismic failure assessments of CVs focused on the performance of un-degraded CVs subject to seismic events and subsequent hazards. Understanding the capacity of CVs that have experienced environmental degradation and are subjected to seismic or other loading is critical, but publications on this topic are still limited in the literature. One study that addressed the effects of environmental degradation on CV integrity under seismic loading is that of Jin et al. [23], who assessed the seismic fragility of a CV with rebar corrosion. They considered the progression of chloride-induced steel corrosion at various stages of the CV service life using a corrosion-rate model and developed seismic fragility functions for each stage. They found that this corrosion reduced the CV's seismic capacity at a high rate early in its service life, but that the capacity reduction stabilized later in the service life primarily due to the stabilization of corrosion propagation in the reinforcing steel. Saouma and Hariri-Ardebili [24] assessed the influence of ASR degradation on the seismic performance of CVs. That study employed a model for ASR progression and the resulting damage and expansion under assumed thermal and moisture conditions to regions of the CV in which the ASR effects were assumed be spatially uniform. The response of the ASR-affected containment was computed under two different synthetic ground motions using arbitrarily selected limit states based on displacements at the top of the structure, and it was found that ASR had a pronounced effect on the seismic fragility, particularly for lower-intensity ground motion. Similar approaches have been applied to simulate the seismic performance of other degraded concrete structures, such as in the work of Nahar et al. [25], which employed a time-dependent model for concrete damage evolution in a concrete gravity dam. Seismic fragility curves were derived from seismic analyses using a set of 30 ground motion records that were applied to the dam at multiple points in time at which varying degradation states were reached. It was found that concrete degradation had a significant effect on seismic fragility with respect to a tensile-damage-based limit state, and a much less pronounced effect on the seismic fragility based on a displacement-based limit state.

The above prior studies of the seismic performance of degraded concrete structures, which represent the current state of the art, all employed degradation models based on assumed progression rates for degradation or assumed conditions such as temperature and moisture that drive degradation. Degradation is expected to have significant spatial variation due to the widely varying conditions experienced across the regions of large structures. Simulating the distribution of degradation in RC structures and accounting for that in assessments of structural capacity is challenging because it generally requires large-scale multiphysics simulations to capture the spatial and temporal variations of temperature, moisture, and other quantities that drive degradation under conditions imposed by the environment. In addition to the challenges inherent in such multiphysics simulations, simulating the response of the structure in the degraded state to seismic or other similar loading poses significant additional computational challenges.

This study employs a parallel-scalable multiphysics simulation code to quantify the effect of ASR on the seismic performance of a representative RC CV using a 3D FE model. The simulation has two stages, with the first stage simulating the processes involved in the time-dependent development of ASR and the resulting damage. A tightly coupled system of partial differential equations was solved to capture the mechanical, thermal, and moisture conditions, all of which are affected by environmental conditions and have a strong effect on local ASR progression. The second stage uses the model from the first stage, with its predicted spatially varying states of damage and ASR-induced swelling, to simulate the seismic performance of the CV in that degraded state. The simulation code employed here has been validated against experimental tests and can simulate the nonuniform distribution of ASR degradation in the structure based on thermal and moisture boundary conditions, and the effect of confinement in the structure. The second-stage model was used repeatedly as the basis for a probabilistic seismic failure analysis, which was performed on the degraded and pristine containment structures with a suite of GMs, employing failure LSs that are defined based on the damage states of the vessel. Due to the model size and the large number of seismic simulations required by the seismic fragility analysis, this study required significant computational resources, which were provided by a high-performance computing cluster.

2. Alkali-Silica Reaction Model Description

To understand the progression of ASR in the CV and its effects on concrete strength degradation requires modeling the physics related to heat and moisture transport, ASR swelling and kinetics, and concrete and rebar mechanical properties. The governing equations and material models that describe these physics are briefly summarized here, and a more in-depth description is provided in Jain et al. [26].

2.1. Concrete Heat and Moisture Transport

Heat transfer in the structure is modeled using the heat equation:

$$\rho C \frac{\partial T}{\partial t} = \nabla \cdot (k \nabla T) + Q \tag{1}$$

where ρ is the density, C is the specific heat, T is the temperature, k is the thermal conductivity, Q is the rate of heat per unit volume generated within the body, and t is time. The governing equation for moisture transport in concrete, following the approach of Xi et al. [27], is:

$$\frac{\partial W}{\partial H}\frac{\partial H}{\partial t} = \nabla \cdot \left(D_h \nabla H\right) \tag{2}$$

where W is the total water content, D_h is the moisture diffusivity, and $H = P_v/P_{vs}$ is the pore relative humidity, where P_v is the vapor pressure and P_{vs} is the saturate vapor pressure, defined in terms of standard atmospheric pressure and temperature by Bary et al. [28].

2.2. Concrete Alkali-Silica Reaction Expansion and Damage

ASR expansion and ASR-induced degradation are modeled using the Saouma and Perotti model [3]. The model enhances the ASR kinetics models proposed by Larive [29] and Ulm et al. [30] by also considering the effect of local stress states. The ASR extent, ξ, is expressed for unrestrained concrete in terms of the ASR-induced volumetric strain, ε, as:

$$\xi(t) = \frac{\varepsilon(t)}{\varepsilon(\infty)} \tag{3}$$

where $\varepsilon(\infty)$ is the volumetric strain upon ASR completion. The following kinetic model describes the evolution of ASR extent $\xi(t)$ with time:

$$\xi(t) = \frac{1 - e^{\left(\frac{-t}{\tau_c}\right)}}{1 + e^{\left(\frac{-t}{\tau_c} + \frac{\tau_L}{\tau_c}\right)}} \tag{4}$$

where τ_L and τ_C are the characteristic and latency time, respectively. These parameters are affected by temperature and, in the case of τ_C, stress. They are adjusted from values at a reference temperature, T_0 by the following:

$$\tau_C(T) = \tau_C\left(T_0\right) e^{\left(U_C\left(\frac{1}{T} - \frac{1}{T_0}\right)\right)} \tag{5}$$

$$\tau_L\left(T, I_\sigma, f_c'\right) = \tau_L\left(T_0\right) f\left(I_\sigma, f_c'\right) e^{\left(U_L\left(\frac{1}{T} - \frac{1}{T_0}\right)\right)} \tag{6}$$

where T is the temperature, T_0 is the reference temperature, σ is the applied stress, f_c' is the uniaxial compressive strength, U_c and U_L are the activation energy constants for characteristic time and latency, respectively, and I_σ is the first invariant of the stress tensor. The function $f\left(I_\sigma, {f_c}'\right)$ accounts for the impeding effect of compressive stresses on ASR. It evaluates to 1.0 if the material is in tension (i.e., $I_\sigma > 0$), and is otherwise defined as $f\left(I_\sigma, {f_c}'\right) = 1 + \alpha I_\sigma/(3{f_c}')$. The factor α is assumed here to be $4/3$ based on experiments of Multon [31].

The incremental volumetric expansion due to ASR, adjusting for the effects of moisture and stress state, is:

$$\Delta\varepsilon^{\mathrm{ASR}}_{\mathrm{vol}}(t) = \Gamma_t\left(f_t', \sigma_I\right) \Gamma_c\left(\bar{\sigma}, f_c'\right) g(H)\, \dot{\xi}(t, T)\, \varepsilon(\infty)\, |_{T=T_0} \tag{7}$$

where f_t' is the tensile strength, σ_I is the maximum principal stress, $\bar{\sigma}$ is the ratio of the hydrostatic stress to the compressive strength, and $\varepsilon(\infty)_{|T=T_0}$ is the maximum free expansion at the reference temperature determined from laboratory tests. Γ_t accounts for the reduction in ASR swelling due to tensile cracking. It evaluates to 1.0 unless the stress exceeds a tensile threshold, upon which it decays with increasing tensile loading. Similarly, Γ_c accounts for the reduction in ASR swelling due to the diffusion of silica gel into microcracks formed under compressive load [31]. It evaluates to 1.0 under tension, and decreases with increasing compressive load. $g(H)$ captures the dependence of gel expansion on the water content within the concrete. These functions are all defined by Saouma and Perotti [3].

Experimental observations [29, 32] indicate greater ASR swelling in directions with lower compressive stress. This is accounted for here using the procedure of Saouma and Perotti [3], which allocates the total volumetric strain across the three principal stress directions using weights W_k for those directions computed using interpolations from uniaxial, biaxial, and triaxial conditions. The volumetric strain increment in each principal stress direction i is calculated with the computed weights as:

$$\Delta\varepsilon^{\mathrm{ASR}}_{vol|i} = W_i \Delta\varepsilon^{\mathrm{ASR}}_{\mathrm{vol}}\ \forall i = \{1, 2, 3\} \tag{8}$$

which are applied in their corresponding directions.

ASR-induced degradation reduces the concrete's tensile strength and elastic stiffness, expressed as an ASR damage index d_{ASR}:

$$\begin{aligned} \mathbb{C} &= \left(1 - d_{\text{ASR}}\right) \mathbb{C}_0 \\ d_{\text{ASR}} &= \left(1 - \beta_C\right) \xi \end{aligned} \tag{9}$$

where $\mathbb{C}$ and $\mathbb{C}_0$ are the damaged and original elastic stiffness of concrete, respectively, and β_C is the residual elastic stiffness and tensile strength after the completion of ASR. Saouma and Perotti [3] reduced only the tensile strength for ASR damage. However, as described in Section 2.4, a modified approach was employed to account for the effect of ASR on strength within the scalar mechanical damage model used here.

2.3. Concrete Creep

The logarithmic viscoelastic creep model by Giorla [33] is used to account for the long-term creep effects due to ASR-induced stresses on concrete. The total strain ε is decomposed into the elastic strain ε_e (fully recoverable upon unloading), the partly recoverable short-term creep strain ε_r, and the irrecoverable long-term creep strain ε_v. The irrecoverable creep strain is linear with the logarithm of time. The strain decomposition is:

$$\boldsymbol{\varepsilon} = \boldsymbol{\varepsilon_e} + \boldsymbol{\varepsilon_r} + \boldsymbol{\varepsilon_v} \tag{10}$$

The stress $\boldsymbol{\sigma}$ relates to the strains through:

$$\boldsymbol{\sigma} = \mathbb{C}_{\boldsymbol{e}} : \boldsymbol{\varepsilon_e} \tag{11}$$

$$\boldsymbol{\sigma} = \mathbb{C}_{\boldsymbol{r}} : \left(\boldsymbol{\varepsilon_r} + \eta_r \dot{\boldsymbol{\varepsilon}}_{\boldsymbol{r}}\right) \tag{12}$$

$$\boldsymbol{\sigma} = \left(1 + \frac{t}{\tau_v}\right) \eta_v \mathbb{C}_{\boldsymbol{e}} : \dot{\boldsymbol{\varepsilon}}_{\boldsymbol{v}} \tag{13}$$

where $\mathbb{C}_{\boldsymbol{e}}$ is the elasticity tensor, $\mathbb{C}_{\boldsymbol{r}}$ is the recoverable elasticity tensor, η_r is the recoverable viscosity, η_v is the long-term viscosity, and τ_v is the long-term characteristic time. The elasticity tensors are computed based on user-supplied Poisson's ratio, Young's modulus, and recoverable Young's modulus. The long-term and recoverable viscosities can optionally be temperature dependent, although that effect is not accounted for in the present study because its effect is minimal at the temperatures considered. The effect of humidity can be accounted for by multiplying the values of $\mathbb{C}_r$ and η_v for a reference humidity by $1/H$ to obtain appropriate values for the current humidity.

2.4. Concrete Damage

The ASR damage in Equation (9) is combined with the mechanical damage resulting from the ASR expansion and other mechanical loadings to the structure. The mechanical damage is modeled with the Mazars damage model [34, 35], which accounts for the stiffness degradation and the softening behavior of the concrete. The scalar damage index d_m is expressed as a combination of tension and compression damage modes:

$$d_m = \alpha_t d_t + \alpha_c d_c \tag{14}$$

where α_t and α_c are coefficients that depend on the strain orientation, and d_t and d_c are damage variables for tension and compression, respectively. The tensile and compressive damage variables are computed as:

$$d_t = 1 - \frac{\kappa_0 \left(1 - A_t\right)}{\kappa} - \frac{A_t}{\exp\left[B_t \left(\kappa - \kappa_0\right)\right]} \tag{15}$$

$$d_c = 1 - \frac{\kappa_0 \left(1 - A_c\right)}{\kappa} - \frac{A_c}{\exp\left[B_c \left(\kappa - \kappa_0\right)\right]} \tag{16}$$

where A_t, A_c, B_t, and B_c are material parameters that affect the shape of the nonlinear response; they are calibrated to match the peak strength and the softening behavior of the concrete for uniaxial tension and compression, respectively, and κ defines the damage evolution threshold. The two damage indices from Equation (9) and Equation (14) are calculated at each integration point in the domain, and a combined damage index d is calculated with a product rule as:

$$d = 1 - \left(1 - d_m\right)\left(1 - d_{\text{ASR}}\right) \tag{17}$$

The strength and stiffness of the concrete are degraded based on this combined damage index. The combined damage index is limited to a value slightly below 1.0 to avoid numerical issues from a complete loss of material strength.

2.5. Rebar Model

Rebar is modeled with one-dimensional truss elements embedded within the concrete domain, with element sizes comparable to those of the solid elements. A constraint is applied to the rebar, which enforces displacement and temperature compatibility between the rebar nodes and the nodes in the concrete matrix. This represents a perfect bond between the concrete and steel, both mechanically and thermally. The mechanical behavior of the truss element is modeled as purely axial with an elastic-perfectly plastic constitutive relationship. Additionally, the truss element also models axial thermal expansion based on the user-supplied coefficient of thermal expansion for the steel.

3. Containment Vessel Model Description

A 3D FE model of a prototypical large, dry CV was developed. This structure serves as a secondary barrier against contaminant release in the event of failure of the primary coolant system in for a pressurized water reactor. The geometry and boundary conditions used in this model are intended to be prototypical, and do not represent any particular reactor or NPP site. The dimensions and rebar configurations of this model are based on a 1:6-scale CV constructed for overpressurization testing at Sandia National Laboratories [8]. Rather than modeling a 1:6-scale structure for this work, it was preferable to model a full-scale structure to appropriately capture the length scales for all considered physical phenomena. Thus, the dimensions and reinforcing configuration of the 1:6-scale CV were scaled up to create a computational model of a full-scale CV.

3.1. Simulation Environment

All simulations were run using BlackBear [36], which is an open-source code for modeling material degradation and its effects on structures, based on the Multiphysics Object-Oriented Simulation Environment (MOOSE) [37]. MOOSE is an open-source framework that facilitates solution of large coupled-physics models. In this study, MOOSE enables simultaneous solution for the displacement, temperature, and relative humidity fields in a single system of equations during the ASR-degradation analysis phase, followed by solution of only the displacement fields during the seismic loading phase. The CV model studied here is moderately sized, but the large numbers of time steps and seismic simulations required significant computational resources. To accelerate these computations, all simulations were run using parallel processing on a high-performance computing cluster.

3.2. Containment Vessel Finite Element Model

Containment vessels are predominantly axisymmetric structures, but they contain large openings to meet various access needs. For simplicity, no openings were considered in the 3D CV model, and aside from the rebar, this model is based on a revolved axisymmetric geometry employing a single symmetry plane, as shown in Figure 1.

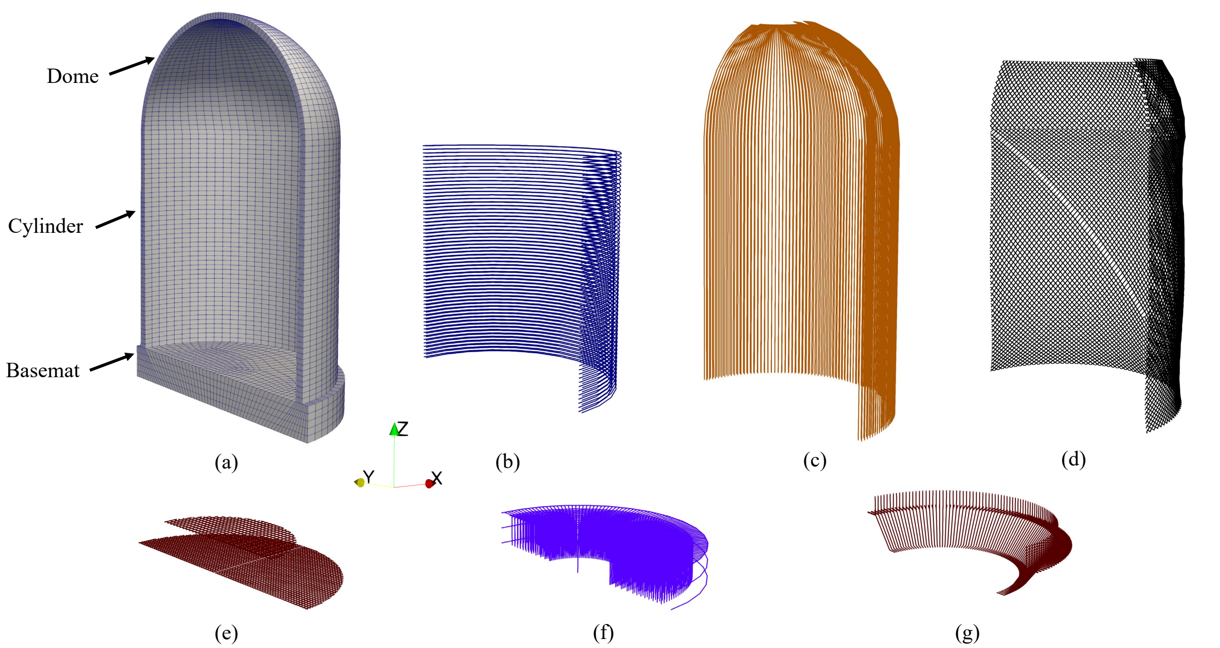

Figure 1: A 3D FE model of an RC CV to simulate ASR-induced volumetric expansion: (a) half-symmetry model of containment; (b) circumferential rebar in the cylindrical part of the structure; (c) meridional rebar; (d) 45°-inclined seismic rebar in basemat, cylinder, and dome; (e) rebar in top and bottom grid in basemat; (f) shear ties and radial and circumferential bars in basemat; and (g) shear ties to connect basemat and cylinder.

The overall height of the CV is 68.0 m, with an inner radius of 20.1 m, a wall thickness of 1.29 m, and a basemat thickness of 6.10 m. The concrete is meshed with eight-noded first-order hexahedral elements, with five elements through the wall thickness, which is generally a minimum refinement level to capture bending behavior with first-order elements. The mesh is coarser in the azimuthal and vertical directions in the walls and dome, with a nominal edge length in those directions of about 0.9 m, compared to an edged length of about 0.3 m in the through-thickness direction. The same rebar arrangement used in the 1:6-scale model is used for the full-scale model, with cross-sectional areas scaled up by a factor of 36 (6^2) to maintain the reinforcement ratio of the scaled model. Individual rebars are modeled as two-noded truss elements. The rebar layout is rather complex, but the model definition is facilitated by the repeating nature of the rebar. In the 1:6-scale model, the rebars terminate at circular plates at the dome apex. Because the plate thickness is not readily available, and that region is not expected to be affected significantly by ASR, the apex plates are not explicitly modeled. That portion of the dome is modeled as being linearly elastic, with a higher stiffness than the surrounding concrete to approximate the effects of the apex plates. The steel liner that typically covers the interior of the CV is not explicitly included in the mesh. Likewise, although the bottom portion of the CV is typically belowground, the stiffening effect of soil is not represented. These assumptions were made to simplify the model, and are conservative because including the liner and the soil in the mechanical model would generally serve to limit lateral displacements during seismic loading.

Because temperature, relative humidity, and displacement affect ASR, all of those fields were solved for on the concrete domain. However, not all of those solutions are relevant for all regions of the model. The relative humidity field was not solved for the rebar. Temperature and displacement fields at the rebar nodes were constrained to match the interpolated values of those fields in the continuum elements. The bottom third of the CV is assumed to be belowground when defining the thermal and moisture boundary conditions. Despite the omission of the soil and liner in the mechanical model, their effects are included in the thermal and moisture boundary conditions as described in Section 3.3 because excluding them would generally make the model less conservative. Including all concrete and rebar elements, the model has approximately 41,000 nodes and 33,000 elements. The coupled system of equations including all field variables has about 190,000 degrees of freedom. This moderate-sized model was used because the seismic fragility analysis requires a large number of simulations, each with a large number of time steps.

3.3. Material Parameters

The material parameters used for modeling the ASR expansion considering thermal transport, moisture transport, and creep are shown in Table 1. Note that while some material parameters are based on those used to validate ASR models against laboratory tests [26], the ASR characteristic and latency times for this model are much longer than those used for simulating laboratory specimens with accelerated ASR. This results in longer times passing before the initial manifestation of the ASR and a slower progression of the ASR, both of which are more realistic outcomes for concrete used in construction. Similarly, to more closely mimic realistic structural concrete properties, the value for the maximum ASR expansion used in this work is an order of magnitude lower than that of the accelerated experiments, which often have uncharacteristically high maximum expansion. Any assessment of an actual structure would need to use parameters specific to the concrete mix used in that structure rather than those from accelerated laboratory tests, which often employ highly reactive concrete mixes.

3.4. Boundary Conditions

Consistent with preliminary work [38], the analysis was performed in two stages: one for the long-term ASR evolution and one for the seismic response. In the first analysis stage, the progression of ASR degradation was modeled

Table 1: Concrete and rebar properties for the CV model.

	Material Property	**Value**
Initial Conditions	Initial relative humidity	80%
	Initial and stress-free temperature	30 °C
Concrete Transport	Heat transport model	Eurocode-2004
	Moisture transport model	Xi
	Aggregate pore type	Dense
	Cement type	U.S. Type II
	Aggregate volume fraction	0.7
	Aggregate mass	1,877 kg/m^3
	Cement mass	354.0 kg/m^3
	Reference density of concrete (ρ)	2,231.0 kg/m^3
	Reference specific heat of concrete (C)	1,100.0 J/(Kg K)
	Water-cement ratio	0.53
ASR Expansion and Damage	Concrete cure time	14 days
	Reference temperature for ASR expansion (T_0)	35 °C
	Max ASR volumetric expansion ($\varepsilon(\infty)$)	0.002
	Characteristic time (τ_C)	750 days
	Latency time (τ_L)	1600 days
	Characteristic time activation energy (U_C)	5,400.0 K
	Latency time activation energy (U_L)	9,400.0 K
	Stress latency factor (α)	1.0
	Compressive stress exponent (β)	1.0
	Expansion stress limit (σ_u)	8.0 MPa
	Tensile retention factor (Γ_r)	1.0
	Tensile absorption factor (Γ_t)	1
	Relative humidity exponent for ASR volumetric strain (m)	1.0
	Compressive strength (f_c')	46.9 MPa
	Tensile strength (f_t')	4.69 MPa
	Fractional residual elastic stiffness (β_C)	0.7
Thermal Expansion	Concrete thermal expansion coefficient	8.0×10^{-6} 1/K
	Rebar thermal expansion coefficient	11.3×10^{-6} 1/K
	Rebar thermal conductivity	45 W/(m K)
Concrete Mechanical	Viscoelastic model	Logarithmic creep
	Concrete Young's modulus	37.3 GPa
	Concrete Poisson's ratio	0.22
	Recoverable Young's modulus	19.9×10^9 GPa
	Recoverable viscosity (η_r)	2.592×10^6 s
	Long-term viscosity (η_v)	1.3824×10^8 s
	Long-term characteristic time (τ_v)	1.3824×10^8 s
	Reference relative humidity for creep (H_{ref})	1.0
	A_t coefficient for Mazars damage	0.9
	A_c coefficient for Mazars damage	1.24
	B_t coefficient for Mazars damage	16,000
	B_c coefficient for Mazars damage	1,200
	Maximum scalar damage	0.99
Rebar Mechanical	Rebar Young's modulus	2.14 GPa
	Rebar yield stress	415 MPa

for 40 years. In the second analysis stage, multiple seismic nonlinear acceleration time histories were applied to the degraded vessel to develop fragility functions.

Kinematic constraints for the ASR degradation analysis include fixed displacements on the bottom surface of the basemat in all directions, as well as fixed displacements on the symmetry plane surface in the direction normal to that surface. Gravity loading is applied throughout the CV volume. For the seismic analysis, the acceleration time history is imposed on the basemat's bottom surface in only one horizontal direction (the y direction, which is the symmetry plane), while the fixed displacements in the other two directions are retained. Prescribing accelerations directly on the CV base is consistent with the assumption that the CV base is on rock.

Relative humidity boundary conditions are prescribed on the outer perimeter of the CV based on climate data for the portion of the containment aboveground, and based on depth-dependent data for the portion belowground. This data was obtained from a U.S. climate station for 2020 [39], and the annual temperature and relative humidity variations are shown in Figure 2. These conditions are repeated annually for the duration of the simulation. The groundwater table is assumed to be 3 m below the soil surface, and a relative humidity of 1.0 is prescribed below that depth. No moisture flux on the interior surface of the CV is assumed because this would be prevented by a steel liner.

Temperatures are prescribed on the exterior surface of the CV using the air and depth-dependent soil data of Figure 2. The air temperatures are adjusted to account for the nonuniform effects of sun exposure and shade on the spatial temperature distribution. The temperatures of the air and concrete in the shade are similar for most parts of the day; however, the temperature of the concrete with direct sun exposure is approximately 16.5 °C higher than the air temperature [40]. It is assumed that temperatures have maximum and minimum values at azimuthal positions of $\theta = 90°$ and $\theta = -90°$, respectively, and linear interpolations between these values are used for other positions according to:

$$T_{\text{conc}} = T_{\text{air}} + (1 + \sin\theta)\,\Delta T_{\text{sun-air}} \tag{18}$$

where T_{conc} is the concrete surface temperature, T_{air} is the air temperature, and $\Delta T_{\text{sun-air}}$ is the difference between the concrete surface and air temperatures. The temperature on the interior surface is prescribed to be a constant 30 °C.

4. Alkali-Silica Reaction Degradation Analysis Results

Upon exposure to the environmental conditions described previously, the RC containment model experienced significant effects from ASR. The temporal and spatial variations in the solutions for quantities that influence ASR as well as ASR-degradation-related quantities can be visualized to understand the behavior of this structure. Solutions for (a) temperature and (b) relative humidity fields are shown in Figure 3 at 10 years (during a summer month with higher air temperatures) and 40 years (during a winter month with lower air temperatures). As observed in the temperature and relative humidity plots, the belowground region has consistently lower temperatures and high relative humidity compared to the rest of the containment throughout the service life of the containment. Likewise, the interior of the containment is exposed to constant elevated temperatures. The seasonal and spatial variation of the temperature occurs in the aboveground outer perimeter of the containment. The plots in Figure 3 also show ASR progression, including (c) contours of the ASR extent, (d) ASR volumetric strain, and (e) total damage. These quantities are shown at 10 years

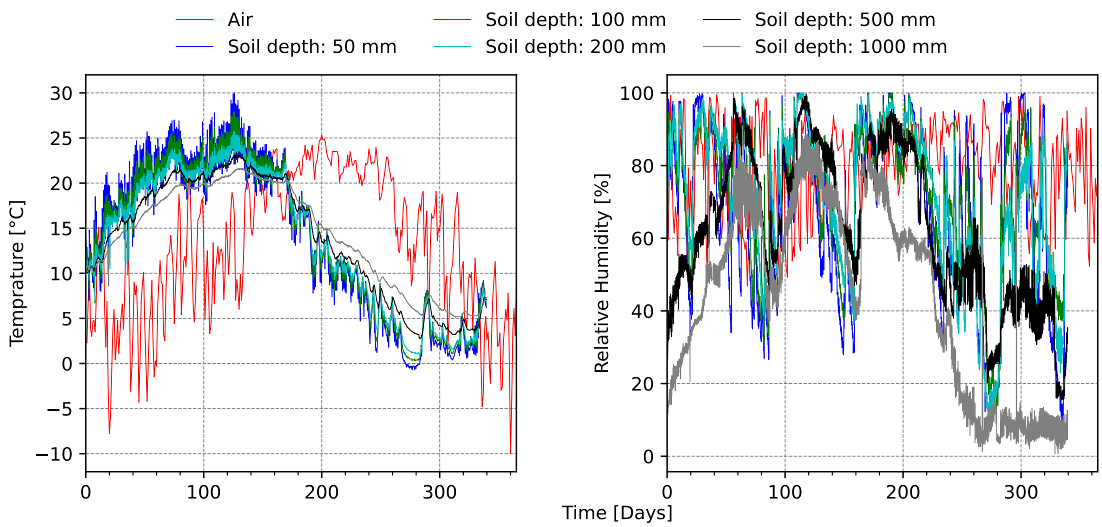

Figure 2: Temperature and relative humidity data from a U.S. climate station used in this simulation [39].

(before the ASR has fully saturated) and 40 years (after the ASR has fully saturated). The total damage contours are the combination of local damage induced by ASR and mechanical damage that occurs due to stresses that exceed the concrete's capacity and could indicate cracking or compressive damage.

After 10 years, the ASR is largely saturated throughout the vessel, except around the outer belowground perimeter, where lower temperatures inhibit the reaction. After 40 years, however, the reaction is essentially complete everywhere. There is spatial variation in the ASR-induced volumetric strain in the interior, and in the below- and above-grade regions of the exterior of the vessel, due to the aforementioned dependencies on stress and moisture. Below-grade regions around the perimeter with higher relative humidity have greater ASR-induced expansion because of this, among other factors. While total damage is shown in Figure 3 (e), the ASR-induced damage is not shown because this damage has a direct correlation with the ASR extent, and the spatial damage distribution is similar to that of the ASR extent. The ASR damage at 40 years is spatially uniform with a value of approximately 0.3, based on the user-prescribed residual stiffness, and all variation in the damage is due to mechanical damage, which is induced primarily by ASR expansion. There is elevated damage around the perimeter of the vessel underground, where there was less ASR early on due to lower temperatures. This is at least partly due to less expansion occurring in these regions, which put them in tension. The nonuniform sun exposure has a noticeable effect on the response, but the ASR effects are relatively minor in the regions affected by sun exposure compared to the ASR-induced damage in the below-grade regions, where ASR is of the greatest concern. Interestingly, damage on the outer surface in the shaded areas of the dome region is greater than that observed in the corresponding sun-exposed areas. This is primarily mechanical damage that progressed early in the simulation when there was greater ASR-induced swelling in surrounding regions. This led to a complex mechanical behavior with elevated bending-induced stresses and the accumulation of damage. This case study highlights the intricate and sometimes counterintuitive nature of how RC structures respond to ASR due to the interactions between physical phenomena.

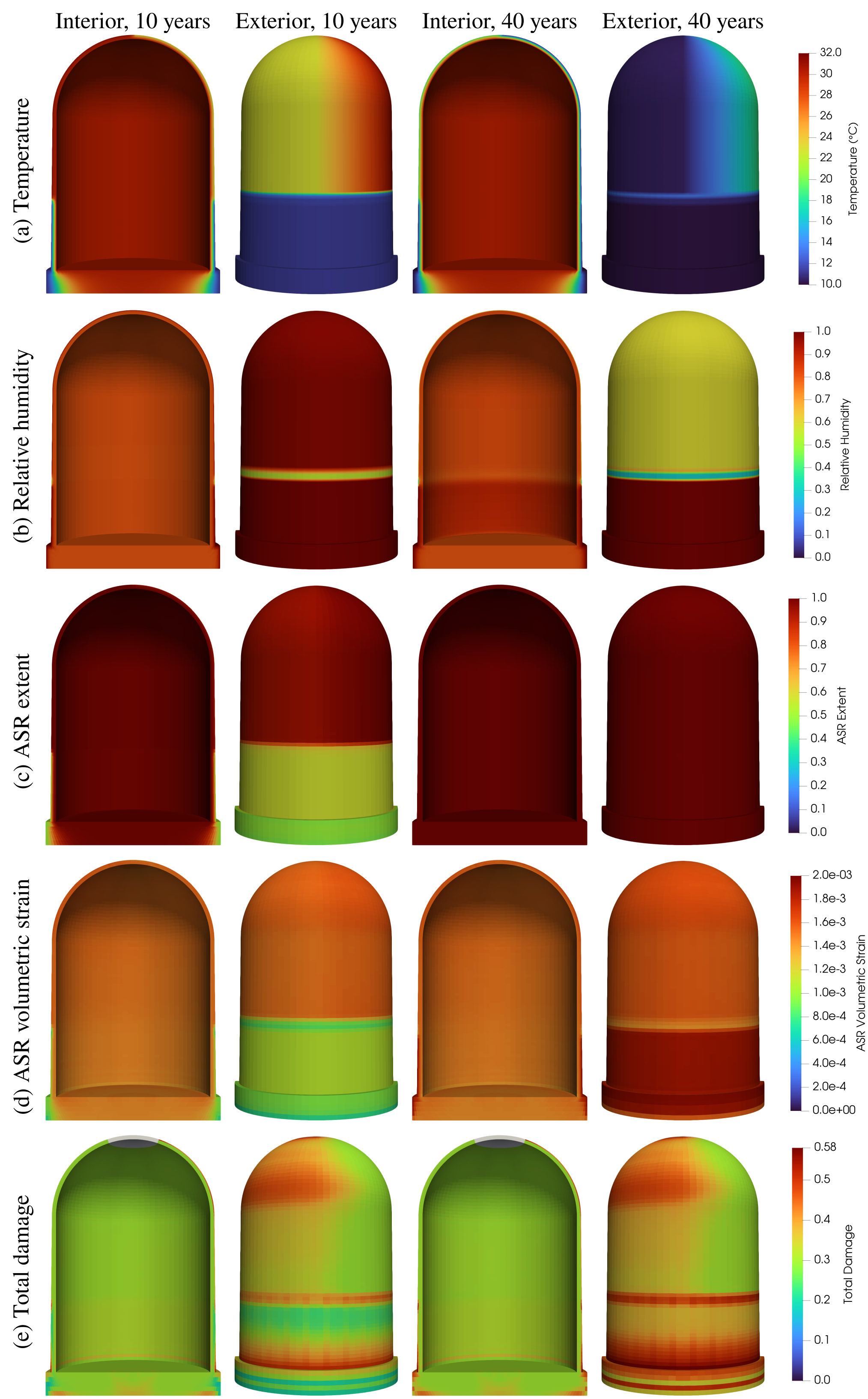

Figure 3: Contours of (a) temperature, (b) relative humidity, (c) ASR extent, (d) ASR volumetric strain, and (e) total damage for the RC CV, showing the response on the inner and outer surface at 10 and 40 years.

5. Seismic Analysis Methodology

Once the CV model was developed for ASR degradation, a number of additional aspects of the model needed to be considered for the seismic simulations, including the processes for initializing the model with the results of the ASR-degradation model, damping, time integration, time stepping, and the seismic fragility analysis, which requires selection of appropriate ground motion and definition of LSs. Details of these considerations are summarized in the following sections.

5.1. Checkpoint and Restart

MOOSE's checkpoint and restart capabilities facilitated the transition from the RC degradation analysis to the seismic nonlinear time history analysis. A checkpoint file output at the end of the degradation analysis contained a snapshot of the numerical model state. This checkpoint file stored the state of the coupled thermal-moisture-mechanical model, which was used to restart the simulation for the seismic simulation, which only modeled mechanical deformation, but which included inertial forces that were not present in the ASR simulation, from the end state of the ASR degradation analysis. This allowed many seismic analyses to be performed concurrently without re-running the degradation analysis.

The fixed-displacement boundary condition applied at the base of the vessel in the degradation analysis in the y direction was replaced by a prescribed acceleration in the restarted seismic analysis. The system needed to be stabilized during the switch of these boundary conditions and the enabling of inertial forces to avoid high-frequency oscillations. This was accomplished using a system in MOOSE that controls which models are active at a given time. The inertial forces were activated at the beginning of the restarted seismic analysis, and the fixed displacements at the vessel's base, which were set throughout the ASR phase, were left active for the first few time steps of the seismic analysis. The fixed displacements were then disabled, and a preset acceleration corresponding to the input GM was applied.

5.2. Structural Damping

Rayleigh damping was used to model the structural damping of the vessel, where the damping matrix (**C**) is proportional to the mass **M** and stiffness **K** respectively as:

$$\mathbf{C} = \eta \mathbf{M} + \zeta \mathbf{K} \tag{19}$$

where η and ζ are the mass- and stiffness-proportional damping parameters, respectively. Modal frequencies of the pristine CV were obtained from an eigenvalue analysis. The damping parameters were calibrated to have a 5% damping ratio for the first and the ninth general mode (the first two lateral translational modes in the direction of the earthquake) with corresponding frequencies of 35 rad/s and 99 rad/s, respectively. The damping parameters calibrated to give the desired 5% damping ratio for these modes are $\eta = 2.604$ and $\zeta = 0.0007$.

5.3. Time Integration

The Hilber-Hughes-Taylor (HHT-α) time-integration scheme was employed to solve the incremental dynamic equation of motion during the seismic analysis. The HHT-α method is a generalization of the Newmark-β time-integration scheme. HHT-α modifies the original equation of motion with a parameter α that induces numerical damping for responses at frequencies above $\frac{1}{2\Delta t}$. The time-integration scheme is unconditionally stable for parameters calculated as $0 \leq \alpha \leq \frac{1}{3}$, $\beta = \frac{(1+\alpha)^2}{4}$ and $\gamma = \frac{1}{2} + \alpha$. For this analysis, the values of these parameters were $\alpha = 0.05$, $\beta = 0.276$, and $\gamma = 0.55$. This set of parameters was found to minimize spurious oscillations and minimally affect the solution in its physical frequency range.

5.4. Adaptive Time Stepping

The time-integration scheme is unconditionally stable for the selected parameters, but limiting the maximum time step size was still desirable for accuracy. To minimize the computational cost of the analysis and ensure solution robustness, the concrete damage used to affect stiffness in the current step is based on the value from the previous step, rather than on the current damage increment. With sufficiently small time steps, the error from this approach can be minimized. This study used an adaptive time-stepping scheme that limited the time step size to limit the damage increment. The size of a given time step was reduced if the increase in integrated damage over the vessel exceeded a user-defined threshold. For the time steps in which the damage increase did not exceed this threshold, the simulation used a default maximum time step size (Δt), also specified by the user. The target time step size Δt_{target} was determined by:

$$\Delta t_{target} = \Delta t \frac{\Delta d}{\Delta d_{target}} V \tag{20}$$

where Δd_{target} is the target maximum value of the damage increase, integrated over the concrete volume. The actual integrated damage increase is Δd, and V is the concrete volume. In this study, $\Delta d_{target} = 5 \times 10^{-4}$ and a default time step size of $\Delta t = 0.01s$ were selected for the seismic analysis based on a sensitivity analysis performed with various damage thresholds and time step sizes for a representative ground motion.

5.5. Seismic Fragility Analysis Procedure

Fragility analysis plays a pivotal role within the seismic probabilistic risk assessment framework by quantifying the failure probability of structures and components under seismic loading. Fragility analysis bridges the gap between seismic hazard analysis and consequence analysis, providing a detailed understanding of how seismic events can impact the integrity of a CV. The fragility function is the probability that the evaluated engineering demand parameter (EDP) exceeds a certain failure LS at a GM intensity measure (IM) x, and can be expressed as a log-normal cumulative distribution function [41]:

$$p\,(\mathrm{EDP} \geq \mathrm{LS}|\mathrm{IM} = x) = \Phi\left(\frac{ln\left(\frac{x}{\theta}\right)}{\beta}\right) \tag{21}$$

where θ and β represent the median capacity and the logarithmic standard deviation of the fragility function, respectively. The fragility function parameters are determined by fitting the IDA data, as discussed in Section 6.2.

5.5.1. *Ground Motion Selection*

The nonlinear structural response is highly sensitive to the characteristics of the applied GM record, and it is essential to apply a variety of GMs to obtain a probabilistic measure of a structure's response. The generic CV does not represent any particular NPP site. Thus, a set of GMs for the fragility analysis were selected from the PEER database [42] according to the following constraints: (1) a magnitude larger than 5.5 moment magnitude (Mw), (2) far-field records with no forward directivity and a minimum site-to-source distance of 10 km, (3) records from sites with shear wave velocity (v_{s30}) greater than 360 m/s (representing at least a class C site classification), (4) a maximum of one record per event to prevent event bias, and (5) the GM should not be scaled by a factor larger than 5.0. The GMs selected from United States Geological Survey sites of Class C [43] or above generally exhibit minimal soil-structure interaction effects, which is consistent with the modeling assumptions. Based on these constraints, 23 GMs were initially chosen for the study, but five records exceeded the scaling factor of 5.0 at failure (Section 5.5.4). The final set of 18 GMs used for the structural evaluation is summarized in Table 2.

Table 2: Ground motion records.

Record	**Event Name**	**Year**	**Station**	**Magnitude (Mw)**	v_{s30} **(m/s)**	**PGA (g)**
1	Kobe	1995	Nishi-Akashi	6.9	609	0.48
2	Hector Mine	1999	Hector	7.1	726	0.34
3	Friuli	1976	Tolmezzo	6.5	505	0.36
4	Parkfield	1966	Temblor pre-1969	6.2	528	0.36
5	San Fernando	1971	Castic–Old Ridge Route	6.6	450	0.32
6	Whittier Narrows	1987	Alhambra–Fremont School	6.0	550	0.29
7	Chi Chi	1999	TCU045	7.6	705	0.47
8	Chuetsu	2007	Iizuna Imokawa	6.8	591	0.63
9	Manjil	1990	Abbar	7.4	724	0.51
10	Niigata	2004	NIG023	6.6	655	0.40
11	Tottori	2000	SMNH02	6.6	503	0.58
12	Sierra Madre	1991	Cogswell Dam–Right Abutment	5.6	680	0.30
13	North Palm Springs	1986	San Jacinto–Soboba	6.1	447	0.25
14	Northridge	1994	Castic–Old Ridge Route	6.7	450	0.57
15	Cape Mendocino	1992	Ferndale Fire Station	7.0	388	0.38
16	New Zealand–02	1987	Matahina Dam	6.6	551	0.28
17	Loma Prieta	1989	Anderson Dam (Downstream)	6.9	489	0.25
18	Darfield	2010	Heathcote Valley Primary School	7.0	422	0.58

5.5.2. *Seismic Damage Analysis of Containment Vessels*

Damage due to ASR is somewhat uniformly distributed over the CV (Section 4), unlike earthquake-induced damage, which is more localized in nature. A wide variety of damage states were predicted for the various GMs and intensity levels simulated here, but many of them had similar characteristics. Figure 4 shows two typical failure modes for the nuclear CV under GM1 (Kobe), showing the total damage distribution. The plots, which are representative of many of these simulations, show the damage field at the end of the time history analysis for one of the simulations run with pristine and degraded vessel conditions. In both cases, damage starts localizing along the CV perimeter, in the cylindrical wall just above where it meets the basemat. In the pristine vessel, damage accumulates in the base and propagates in the vertical direction as the time history analysis progresses. A shear failure mode is observed for all the pristine vessel cases. A second type of damage distribution shown in Figure 4 is typical for the degraded vessel. The seismic simulation starts with a somewhat uniform baseline damage level due to ASR. As the earthquake progresses, damage starts accumulating in the dome section of the structure, and there is reduced damage localization at the base relative to the pristine vessel. The localized damage at the base progresses upward diagonally.

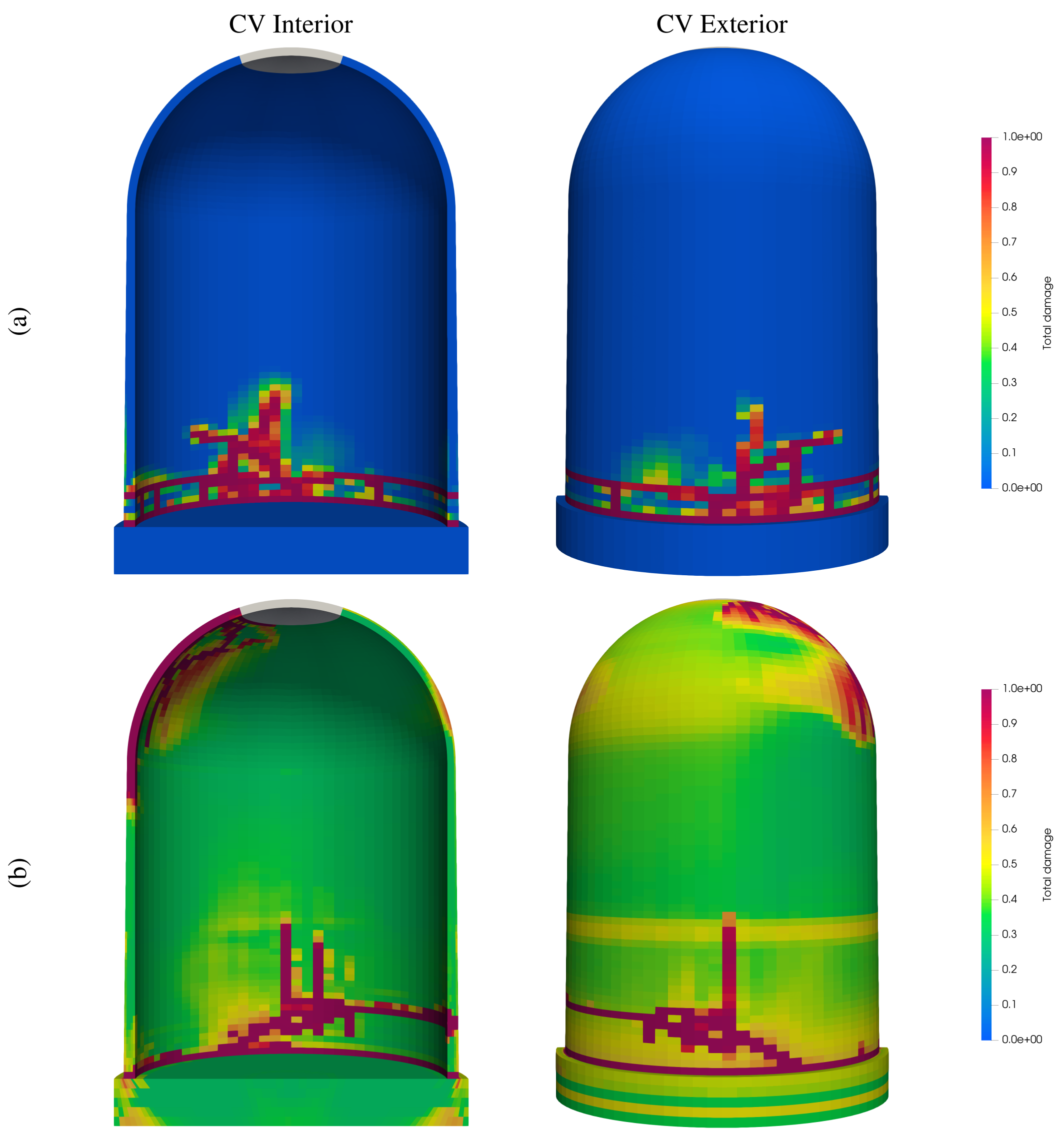

Figure 4: Spatial distribution of damage for a (a) pristine vessel and a (b) degraded vessel subjected to GM1 (Kobe).

5.5.3. *Failure Limit States*

The fragility function defined by Equation (21) requires that a performance LS be defined, usually in terms of a certain EDP associated with a specific damage level or structural failure. The performance LSs used for civil RC structures and components are not easily transferable to CVs. Failure LSs for CVs have been conventionally defined in terms of either "drift ratio" as EDP [14, 18, 23] based on performance LSs for shear walls in nuclear systems and components [44], or as damage indices [17, 19]. However, these LSs are not defined for containment walls, whose scale and design differ significantly from conventional shear walls. An alternative approach more applicable to CVs is to define a performance LS based on whether the strain at local regions in the containment structure exceeds the concrete cracking strain [45]. Defining failure based on whether some local point in the large containment structure reaches cracking strain could be a suitable EDP for a functional LS, such as leak tightness, but it is not indicative of the potential for structural failure of the containment.

In this study, failure LSs are defined based on a static pushover analysis of the CV where containment top displacements are associated to performance goals [46, 47, 48]. To study the CV behavior under a pushover scenario, a monotonically increasing inverted triangular body force (increasing in magnitude with increasing elevation) was applied to the pristine CV model, and the stresses and strains in the concrete and rebar were monitored. Four LSs were then defined by correlating the relative displacement of the containment top node from the pushover analysis to specific performance goals. The first two LSs, concrete cracking and rebar yielding at any material point (LS1 and LS2, respectively), define functional failure of the containment, at which point its ability to maintain leak tightness could be compromised because the strains in the concrete could be sufficient to cause a tear in the steel liner, which would likely be relatively small at LS1 since that is the point of first concrete fracture. The following two LSs (LS3 and LS4) represent moderate and extensive cracking in the concrete, respectively, and are associated with potential structural failure of the RC containment. LS3 is defined as the point when the concrete loses 50% of its compressive strength during the pushover analysis at any material point, and LS4 is defined as when concrete loses 85% of its strength at any material point in the pushover analysis. Figure 5 shows the pushover capacity curve for the containment structure with associated damage distribution at each LS.

Table 3 lists the threshold containment top displacements in the for each LS. During a seismic time history analysis, these top node displacements are assumed to correspond to the above four LSs. The LSs employed here indicate when certain damage levels are reached, and give some indication of when leak-tightness may be a concern, but these do not directly indicate when leakage or rupture during overpressurization. The work of Petti et al. [49] previously demonstrated the usage of leakage and rupture criteria in overpressurization simulations of degraded CVs. Similar procedures should be applied to the CV following the seismic simulations performed here, to provide more direct indications of limit states with direct applicability to assessing risk of contaminant release, but are outside the scope of the present effort.

Table 3: Limit states for containment top displacements.

Limit State (LS)	LS1	LS2	LS3	LS4
Displacement (m)	0.020	0.031	0.042	0.065

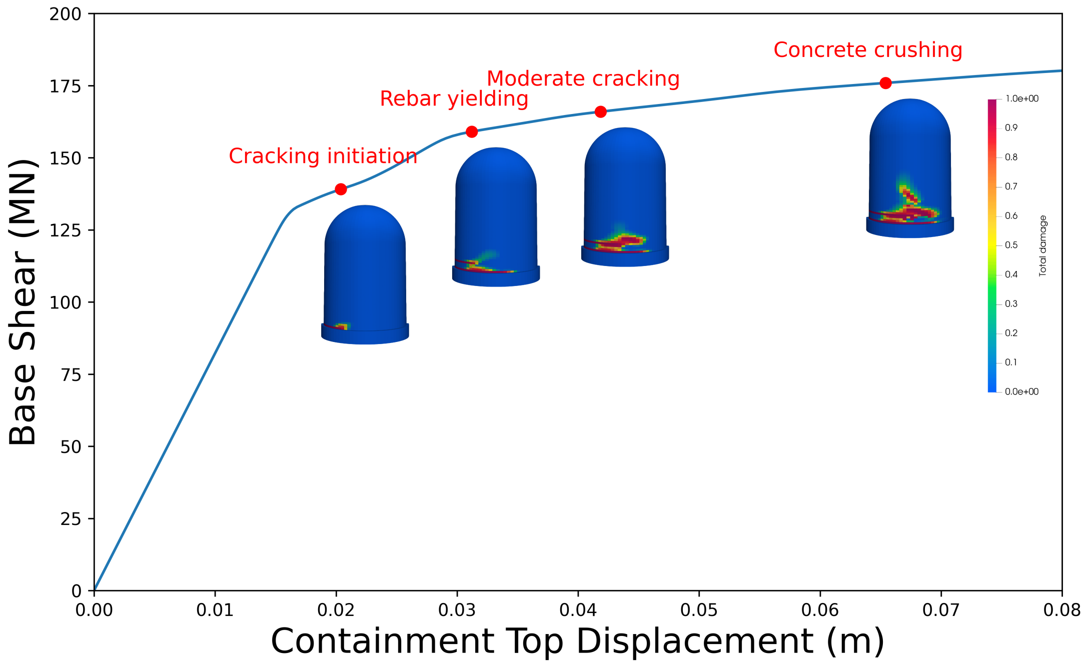

Figure 5: Pushover capacity curve (base shear vs. displacement) with failure LSs, indicating the four LSs used in this study along with the corresponding total damage contours in those models.

5.5.4. Intensity Measure Selection

An appropriate IM selection is essential to minimize the variability in structural response with different GMs. The spectral acceleration at the first mode period ($S_a(T_1)$) is commonly used because it correlates the structural response for structures with a first-mode-dominated response. However, this IM cannot directly account for a higher mode response and nonlinear behavior. Moreover, the fundamental period of the containment structure elongates from the pristine CV case to the degraded vessel. To account for these effects, this study used the 5% damped average spectral acceleration $S_{a,av}$ over a period range from $0.2T_1 = 0.036\ s$ to $2T_1 = 0.36\ s$ as the IM for the IDA [50, 51], where $T_1 = 0.18\ s$ is the first mode period of the pristine CV. The average value is the geometric mean of the spectral accelerations over the period range.

6. Seismic Fragility Analysis Results

Once the LSs and IMs are defined, IDAs were performed using the set of 18 GM records, and fragilities were determined from the IDA results, as described in the following sections. This process required running a large number of simulations. The number of time steps varied by simulation, but each seismic model typically required around 1,000–2,000 steps. Each of the 18 GM records was run at monotonically increasing levels of the $S_{a,av}$ IM until failure was reached for both the degraded and the intact CV. In total, 649 seismic models were run to obtain the IDA plots. All individual models were run on 96 processor cores of a high-performance computing cluster, and typically required about 50 hours to complete, although some models with extensive damage required significantly more computational time. The full set of models presented here required over 3 million core-hours of computational time on a high-performance computing cluster.

6.1. Incremental Dynamic Analysis Results

The IDA was performed by scaling the GMs to incremental values of average spectral accelerations. Figure 6 shows the IDA results for the pristine and degraded CVs for the 18 GM records, as well as the 16th and 84th percentile curves. The four LSs discussed in Section 5.5.3 are represented by vertical dotted blue lines. The IDA results show a softer linear slope at the start of the IDA curves for the degraded vessels due to the ASR degradation. The initial linear stiffness of the median IDA curve of the pristine vessel is about 1.5 times the initial stiffness of the median IDA curve of the degraded vessel, which corresponds to about a 22% variation in the fundamental period of the structure.

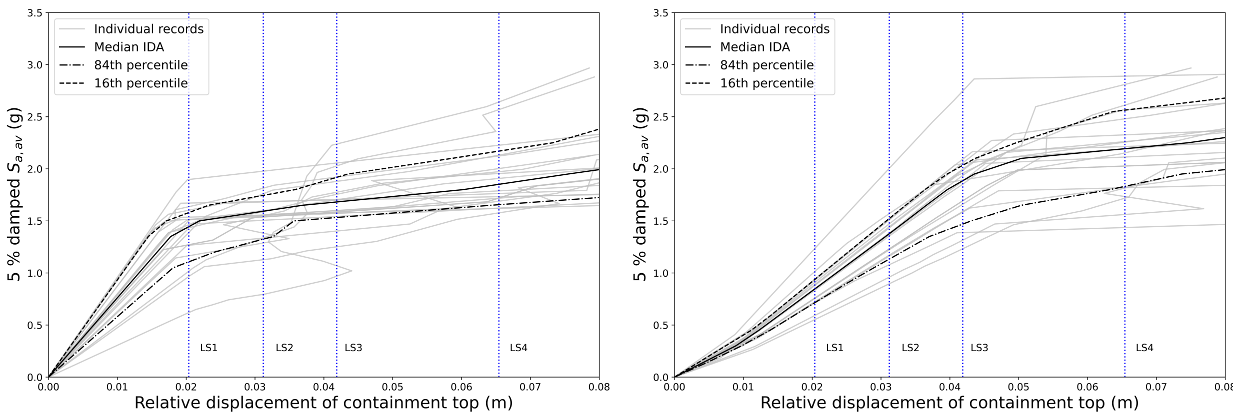

(a)

(b)

Figure 6: Incremental dynamic analysis curves for a (a) pristine and a (b) degraded vessel.

6.2. Fragility Fitting

The fragility function parameters in Equation (21) are estimated using the maximum likelihood estimation (MLE) method [52]. Assuming that the observation of failure at a particular LS at a given intensity measure IM $= x$ is independent for each GM record, the probability of observing m failures in n total observations can be estimated by a binomial distribution:

$$P = \binom{n}{m} p(x)^m (1 - p(x))^{n-m} \tag{22}$$

where $\binom{n}{m}$ is the binomial coefficient given by $\frac{n!}{m!(n-m)!}$, and $p(x_i)$ is the probability of failure at intensity level x, given by the fragility function in Equation (21). Substituting the expression for the fragility function in Equation (22) yields:

$$P = \binom{n}{m} \left[\Phi\left(\frac{ln(x/\theta)}{\beta}\right)\right]^m \left[1 - \Phi\left(\frac{ln(x/\theta)}{\beta}\right)\right]^{n-m} \tag{23}$$

where θ and β represent the median seismic capacity and logarithmic standard deviation as defined in Equation (21). Then, the likelihood function for observing the failures at multiple intensity levels can be expressed as the product of individual binomial probabilities for each intensity measure:

$$L = \prod_{j=1}^{r} \binom{n_j}{m_j} \left[\Phi\left(\frac{ln\left(x_j/\theta\right)}{\beta} \right) \right]^{m_j} \left[1 - \Phi\left(\frac{ln\left(x_j/\theta\right)}{\beta} \right) \right]^{n_j - m_j} \tag{24}$$

where r is the number of intensity levels. The likelihood function (likelihood of the given fragility function resulting from observed IDA data—i.e., observed failures at IM levels) can then be maximized to calculate the optimized fragility function parameters. The optimization is performed using a Python script that maximizes the logarithm of the likelihood function in Equation (24):

$$\max_{\hat{\theta},\hat{\beta}} \left\{ \sum_{j=1}^{r} \binom{n_j}{m_j} + m_j \left[\Phi\left(\frac{ln\left(x_j/\theta\right)}{\beta} \right) \right] + \left(n_j - m_j\right) \left[1 - \Phi\left(\frac{ln\left(x_j/\theta\right)}{\beta} \right) \right] \right\} \tag{25}$$

Table 4 lists the median seismic capacity and the dispersion at the LSs following the optimization fitting, and Figure 7 shows fitted fragility functions for the pristine and degraded CVs, respectively. The median capacity for the cracking initiation (LS1) is 0.8 g for the degraded vessel, which is 40% lower than the median capacity for the pristine vessel (1.3 g). The median capacity for LS2 is also smaller for the degraded vessel (1.3 g) compared to the pristine one (1.5 g). However, for the structural limit states LS3 and LS4, the median capacity is slightly larger for the degraded vessel compared to the pristine vessel. The median capacities are 1.7 g and 1.8 g for the pristine and degraded vessels at LS3, respectively, and 1.9 g and 2.1 g at LS4. Figure 8 compares the fragility curves for the vessels at the functional (LS1 and LS2) and structural (LS3 and LS4) limit states. The fragility curves of the degraded vessel are visibly separated from the those of the pristine vessel. The probability of failure at a certain intensity level for these LSs is much higher for the degraded vessel than for the pristine one. This observation indicates that ASR-degraded vessels have a greater risk of releasing contaminants through a tear in the liner than do pristine vessels under lower-intensity earthquakes. However, for the structural LSs (LS3 and LS4), the effect of ASR degradation is not as significant, and the median capacities are similar for both the pristine and degraded cases.

The finding that degradation has a larger effect on the median capacity at the lower limit states than on the higher limit state is consistent with the results of Saouma and Hariri-Ardebili [24] for ASR-affected CVs and Nahar et al. [25] for concrete gravity dams. While the capacity at the higher LSs is similar for the degraded and pristine vessels, the dispersion is larger for the degraded vessel (0.14 versus 0.19 for LS3, and 0.14 versus 0.19 for LS4 for the pristine and degraded vessels, respectively). Inspection of the IDA curves in Figure 6 helps explain these findings. It is evident that at low intensity the CV is in a largely elastic regime in both the pristine and degraded cases. As would be expected due to the presence of distributed ASR damage, the degraded CV is more compliant than the pristine containment. The pristine CV transitions from an elastic to an inelastic response around LS1, but that transition happens at a much higher displacement (around LS3) for the degraded CV. Once the seismic intensity exceeds this transition point, the IDA curves for both cases are relatively flat, with large increases in displacement corresponding to small increases in seismic intensity. The median seismic intensities for LS1 and LS2 differ significantly for the pristine and degraded case because the degraded case is in its elastic regime at both of those LSs, while the pristine case has already reached its elastic limit at LS1. There is a smaller difference in the seismic intensity level corresponding to the inelastic regime for the pristine and degraded case, probably because the response at that point is driven more by the response of the rebar than of the concrete. The response of the degraded CV has greater variation than that of the pristine CV at high seismic intensity, likely due to the greater damage extent in the degraded CV.

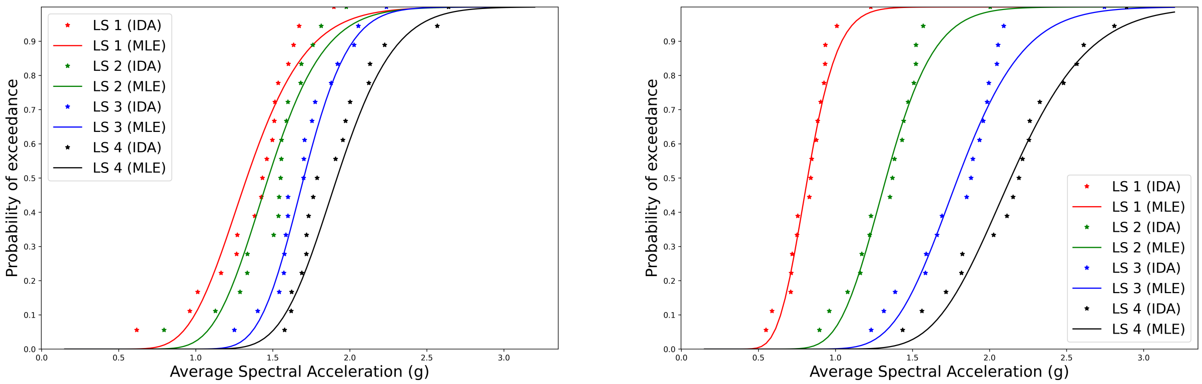

(a) (b)

Figure 7: Fitted fragility curves for a (a) pristine vessel and a (b) degraded vessel.

Table 4: Fragility parameters for the CVs.

	Pristine Vessel		Degraded Vessel	
	θ	β	θ	β
LS1	1.3g	0.23	0.8g	0.19
LS2	1.5g	0.19	1.3g	0.19
LS3	1.7g	0.14	1.8g	0.19
LS4	1.9g	0.15	2.1g	0.19

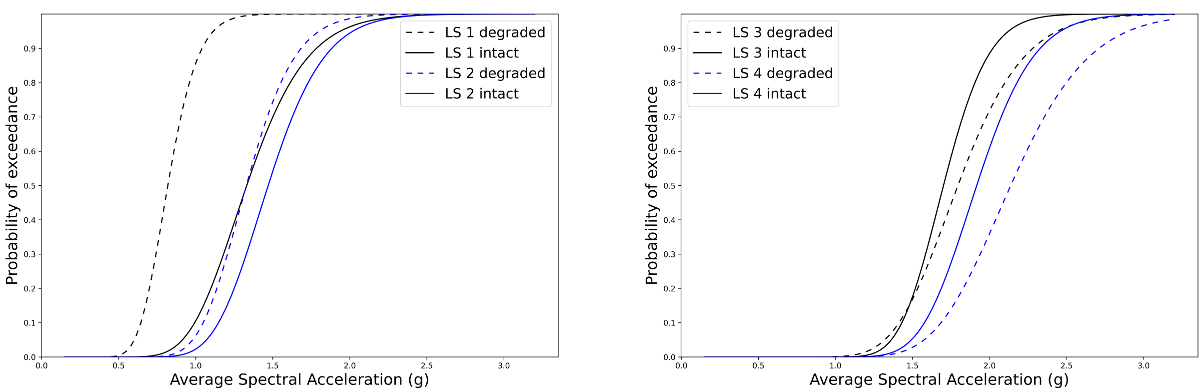

(a) (b)

Figure 8: Comparison of fragility curves for (a) functional LSs and (b) structural LSs.

7. Summary and Conclusions

This study assessed the effects of aging deterioration on the seismic capacity of a generic nuclear reinforced concrete containment vessel (CV). A multiphysics simulation of age-related degradation induced by alkali-silica reaction (ASR) and its effects on seismic capacity was performed for a full-scale reinforced concrete nuclear CV. The degradation model predicted the evolution of ASR and ASR-induced expansion and damage, driven by predictions of spatially resolved thermal, moisture, and deformation. This degradation model provided the initial spatially resolved conditions for seismic simulations of the aged CV. The seismic capacity of the aged vessel was evaluated using an incremental dynamic analysis (IDA) seismic evaluation. Seismic fragility functions for the CV, both pristine and degraded, were developed using maximum likelihood estimation of the IDA data. The failure limit states (LSs) were defined based on a pushover analysis. The following conclusions can be drawn from the ASR and seismic models:

1. The initial rate of ASR progression and expansion is delayed in the below-grade region of the CV due to lower temperatures in the region. The ASR eventually reaches its full extent everywhere in the vessel, but the ASR-induced expansion varies spatially due to dependence on local stress and humidity. The load redistribution resulting from non-uniform expansion caused mechanical damage, which was concentrated in a few regions, including in the outer perimeter of the cylinder just above the junction with the basemat and the above-grade region of the containment with less sun exposure.
2. The base of the CV is vulnerable during earthquakes; localized damage initiated in this region for both the intact and degraded vessels under seismic excitation. For the pristine vessel, the damage generally localizes around the base of the cylinder. The presence of ASR-induced degradation, however, alters the locations of damage localization. Damage in the ASR-degraded CVs tended to propagate upward from the base in a diagonal manner, and damage also accumulated in the dome portion of the vessel.
3. The presence of ASR significantly reduces the seismic capacity of the vessel for the functional LSs, which represents the initiation of cracking and rebar yielding. The median capacity for LS1, which corresponds to crack initiation, decreased by approximately 40% for the ASR-degraded containment. This potentially indicates a higher likelihood of containment leakage if the containment were subjected to pressurization following an earthquake. However, leakage would only occur if the steel liner were to rupture. An analysis of the containment under overpressurization following the seismic event, including the effects of the liner, would be required to fully assess the importance of the reduction of capacity at these lower LSs.
4. The median capacities for the structural collapse LSs were comparable for pristine and degraded vessels. The median capacities for LS4 were 1.9 g and 2.1 g for the pristine and degraded vessels, respectively. The dispersion in the fragility curve of the degraded curve was larger, however, indicating that ASR degradation results in a higher degree of uncertainty.

In addition to these findings, this work also demonstrates the applicability of an open-source, multiphysics, parallel simulation code to model degradation and its effects on complex RC structures. The CV model had considerable complexity due to its explicit representation of rebars and use of coupled-physics models. The use of high-performance computing resources significantly benefited this effort by accelerating the individual simulations and running large batches of seismic simulations. While this framework is largely feature-complete for capturing the major important mechanisms, further development in areas such as more sophisticated concrete and steel constitutive models and models for bond slip between concrete and rebar could improve the accuracy of this model. Further validation, particularly on the effects of ASR on mechanical capacity, would improve confidence in this modeling approach and framework.

8. Acknowledgments

This research was supported by the Nuclear Safety Research and Development (NSR&D) program of the U.S. Department of Energy's Office of Environment, Health, Safety and Security. Foundational capabilities were developed by the U.S. Department of Energy's Light Water Reactor Sustainability and Nuclear Energy Advanced Modeling and Simulation programs. This research utilized the resources of the High Performance Computing Center at Idaho National Laboratory, which is supported by the Office of Nuclear Energy of the U.S. Department of Energy and the Nuclear Science User Facilities under contract no. DE-AC07-05ID14517. This manuscript was authored by Battelle Energy Alliance, LLC under contract no. DE-AC07-05ID14517 with the U.S. Department of Energy. The U.S. Government retains a nonexclusive, paid-up, irrevocable, worldwide license to publish or reproduce the published form of this manuscript, or allow others to do so, for U.S. Government purposes.

References

[1] H. Graves, Y. Le Pape, D. Naus, J. Rashid, V. Saouma, A. Sheikh, and J. Wall. Expanded Materials Degradation Assessment (EMDA) Volume 4: Aging of concrete and civil structures. Technical Report NUREG/CR-7153, Vol. 4, ORNL/TM-2013/532, Oak Ridge National Laboratory, Oak Ridge, TN, October 2014. URL `http://www.nrc.gov/reading-rm/doc-collections/nuregs/contract/cr7153/v4/`.

[2] D.J. Naus, C.B. Oland, B.R. Ellingwood, H.L. Graves, and W.E. Norris. Aging management of containment structures in nuclear power plants. *Nuclear Engineering and Design*, 166(3):367–379, 1996. ISSN 0029-5493. doi: 10.1016/S0029-5493(96)01254-X. Topical Issue on The Third International Conference on Containment Design and Operation.

[3] V. Saouma and L. Perotti. Constitutive model for alkali-aggregate reactions. *ACI Materials Journal*, 103(3), 2006. doi: 10.14359/15853.

[4] U.S. Nuclear Regulatory Commission. Special NRC oversight at Seabrook nuclear power plant: Concrete degradation, 2012. URL `https://www.nrc.gov/reactors/operating/ops-experience/concrete-degradation.html`.

[5] R. Manabe, H. Kawae, K. Ogawa, and M. Matsuura. Maintenance management of turbine generator foundation affected by alkali–silica reaction. *Journal of Advanced Concrete Technology*, 14(9):590–606, 2016. doi: 10.3151/jact.14.590.

[6] A. C. Eberhardt, C. A. Jones, C. T. Smith, and O. Jovall. *Code for Concrete Containments*, chapter 15. ASME Press, January 2020. doi: 10.1115/1.861981_ch15.

[7] *ASME Boiler and Pressure Vessel Code, Section III, Rules for Construction of Nuclear Facility Components, Division 2, Code for Concrete Containments*. Number ASME BPVC.III.2-2023. ASME, 2023.

[8] D. B. Clauss. Round-robin pretest analyses of a 1:6-scale reinforced concrete containment model subject to static internal pressurization. Technical Report NUREG/CR-4913, SAND87-0891, Sandia National Laboratories, Albuquerque, NM, May 1987.

[9] M. F. Hessheimer and R. A. Dameron. Containment integrity research at Sandia National Laboratories. Technical Report NUREG/CR-6906 SAND2006-2274P, Sandia National Laboratories, Albuquerque, NM, July 2006. URL `https://www.nrc.gov/docs/ML0624/ML062440075.pdf`.

[10] T. Hirama, M. Goto, T. Hasegawa, M. Kanechika, T. Kei, T. Mieda, H. Abe, K. Takiguchi, and H. Akiyama. Seismic proof test of a reinforced concrete containment vessel (RCCV): Part 1: Test model and pressure test. *Nuclear Engineering and Design*, 235(13):1335–1348, 2005. doi: 10.1016/j.nucengdes.2005.01.002.

[11] J. Liu, J. Kong, and X. Kong. Shaking table model tests of concrete containment vessel (CCV) for CPR1000 nuclear power plant. *Progress in Nuclear Energy*, 93:186–204, 2016. doi: 10.1016/j.pnucene.2016.08.016.

[12] S. G. Cho and Y. H. Joe. Seismic fragility analyses of nuclear power plant structures based on the recorded earthquake data in Korea. *Nuclear Engineering and Design*, 235(17):1867–1874, 2005. doi: 10.1016/j.nucengdes.2005.05.021.

[13] I.-K. Choi, Y.-S. Choun, S.-M. Ahn, and J.-M. Seo. Seismic fragility analysis of a CANDU type NPP containment building for near-fault ground motions. *KSCE Journal of Civil Engineering*, 10(2):105–112, March 2006. doi: 10.1007/bf02823928.

[14] T. K. Mandal, S. Ghosh, and N. N. Pujari. Seismic fragility analysis of a typical Indian PHWR containment: Comparison of fragility models. *Structural Safety*, 58:11–19, 2016. doi: 10.1016/j.strusafe.2015.08.003.

[15] N. Nakamura, N. Yabushita, T. Suzuki, J. Yamada, N. Tsunashima, and T. Nakano. Analyses of reactor building by 3D nonlinear FEM models considering basemat uplift for simultaneous horizontal and vertical ground motions. *Nuclear Engineering and Design*, 238(12):3551–3560, 2008. doi: 10.1016/j.nucengdes.2008.06.005.

[16] N. Nakamura, S. Akita, T. Suzuki, M. Koba, S. Nakamura, and T. Nakano. Study of ultimate seismic response and fragility evaluation of nuclear power building using nonlinear three-dimensional finite element model. *Nuclear Engineering and Design*, 240(1):166–180, 2010. doi: 10.1016/j.nucengdes.2009.10.018.

[17] S. Jin and J. Gong. Damage performance based seismic capacity and fragility analysis of existing concrete containment structure subjected to near fault ground motions. *Nuclear Engineering and Design*, 360:110478, 2020. doi: 10.1016/j.nucengdes.2019.110478.

[18] Song Jin, Hua Rong, and Xuetao Lyu. Probabilistic seismic performance evaluation of nuclear containment structure subjected to far-fault ground motions. *Structures*, 32:2232–2246, 2021. doi: 10.1016/j.istruc.2021.04.013.

[19] X. Bao, M.-H. Zhang, and C.-H. Zhai. Fragility analysis of a containment structure under far-fault and near-fault seismic sequences considering post-mainshock damage states. *Engineering Structures*, 198:109511, 2019. doi: 10.1016/j.engstruct.2019.109511.

[20] X. Bao, L. Jin, J. Liu, and L. Xu. Framework for the mainshock-aftershock fragility analysis of containment structures incorporating the effect of mainshock-damaged states. *Soil Dynamics and Earthquake Engineering*, 153:107072, 2022. doi: 10.1016/j.soildyn.2021.107072.

[21] S. Jin, D. Jiang, D. Wang, S. Wang, and Z. Wang. Fragility evaluation of nuclear containment structure subjected to earthquake and subsequent internal pressure. *Annals of Nuclear Energy*, 197:110257, 2024. doi: 10.1016/j.anucene.2023.110257.

[22] F. Lin and H. Li. Safety analysis of nuclear containment vessels subjected to strong earthquakes and subsequent tsunamis. *Nuclear Engineering and Technology*, 49(5):1079–1089, 2017. doi: 10.1016/j.net.2017.03.008.

[23] S. Jin, D. Wang, D. Jiang, and Q. Zhang. Seismic fragility analysis of nuclear containment structure under chloride-induced reinforcing steel corrosion conditions. *Annals of Nuclear Energy*, 192:109989, 2023. doi: 10.1016/j.anucene.2023.109989.

[24] V. E. Saouma and M. A. Hariri-Ardebili. Seismic capacity and fragility analysis of an ASR-affected nuclear containment vessel structure. *Nuclear Engineering and Design*, 346:140–156, 2019. doi: 10.1016/j.nucengdes.2019.02.011.

[25] T. T. Nahar, A.-T. Cao, and D. Kim. Risk assessment of aged concrete gravity dam subjected to material deterioration under seismic excitation. *International Journal of Concrete Structures and Materials*, 14(1), October 2020. doi: 10.1186/s40069-020-00430-z.

[26] A. Jain, B. W. Spencer, A. Dahal, S. Biswas, and S. L. N. Dhulipala. Multiphysics simulation of recent experiments on alkali-silica reaction expansion in reinforced concrete members. *In Review*.

[27] Y. Xi, Z. P. Bažant, L. Molina, and H. M. Jennings. Moisture diffusion in cementitious materials Moisture capacity and diffusivity. *Advanced Cement Based Materials*, 1(6):258–266, November 1994. doi: 10.1016/1065-7355(94)90034-5.

[28] B. Bary, M. V. G. de Morais, S. Poyet, and S. Durand. Simulations of the thermo-hydro-mechanical behaviour of an annular reinforced concrete structure heated up to 200°C. *Engineering Structures*, 36:302–315, March 2012. doi: 10.1016/j.engstruct.2011.12.007.

[29] C. Larive. *Apports Combin'es de l'Experimentation et de la Modélisation à la Comprehension del' A lcali-Réaction et de ses Effets Mécaniques,*. PhD thesis, Laboratoire Central des Ponts et Chaussées, Paris., 1998.

[30] F.-J. Ulm, O. Coussy, L. Kefei, and C. Larive. Thermo-Chemo-Mechanics of ASR Expansion in Concrete Structures. *Journal of Engineering Mechanics*, 126(3):233–242, March 2000. doi: 10.1061/(ASCE)0733-9399(2000)126:3(233).

[31] S. Multon. *Experimental and theoretical evaluation of mechanical effects of alkali-silica reaction on laboratory structures*. PhD thesis, Marne-la-Vallée, 2003.

[32] S. Multon and F. Toutlemonde. Effect of applied stresses on alkali–silica reaction-induced expansions. *Cement and Concrete Research*, 36(5):912–920, 2006. doi: 10.1016/j.cemconres.2005.11.012.

[33] A. Giorla. Implementation of concrete creep model in Grizzly. Technical Report ORNL/TM-2017/729, Oak Ridge National Laboratory, Oak Ridge, TN, November 2017.

[34] J. Mazars. *Application de la mécanique de l'endommagement au comportement non linéaire et à la rupture du béton de structure*. PhD thesis, Université Paris 6, France, 1984.

[35] G. Pijaudier-Cabot and J. Mazars. Damage models for concrete. In J. Lemaitre, editor, *Handbook of Materials Behavior Models*. Academic Press, 2001.

[36] B. W. Spencer, W. M. Hoffman, S. Biswas, W. Jiang, A. Giorla, and M. A. Backman. Grizzly and BlackBear: Structural component aging simulation codes. *Nuclear Technology*, 207(7):981–1003, 2021. doi: 10.1080/00295450.2020.1868278.

[37] G. Giudicelli et al. 3.0 - MOOSE: Enabling massively parallel multiphysics simulations. *SoftwareX*, 26:101690, May 2024. doi: 10.1016/j.softx.2024.101690.

[38] S. L. Dhulipala, A. Dahal, B. Spencer, Amit Jain, A. Batikh, and M. Diaconeasa. Preliminary nuclear containment vessel modeling for multi-hazard probabilistic risk assessment under seismic hazards and concrete degradation. In *18th International Probabilistic Safety Assessment and Analysis (PSA 2023)*, PSA 2023. American Nuclear Society, 2023. doi: 10.13182/psa23-41001.

[39] J. E. Bell, M. A. Palecki, C. B. Baker, W. G. Collins, J. H. Lawrimore, R. D. Leeper, M. E. Hall, J. Kochendorfer, T. P. Meyers, T. Wilson, and H. J. Diamond. U.s. climate reference network soil moisture and temperature observations. *Journal of Hydrometeorology*, 14(3):977 – 988, 2013. doi: 10.1175/JHM-D-12-0146.1.

[40] D. Armson, P. Stringer, and A. R. Ennos. The effect of tree shade and grass on surface and globe temperatures in an urban area. *Urban Forestry & Urban Greening*, 11(3):245–255, 2012. doi: 10.1016/j.ufug.2012.05.002.

[41] R. P. Kennedy and M. K. Ravindra. Seismic fragilities for nuclear power plant risk studies. *Nuclear Engineering and Design*, 79(1):47–68, 1984. doi: 10.1016/0029-5493(84)90188-2.

[42] Pacific Earthquake Engineering Research Center. PEER ground motion database. URL `https://ngawest2.berkeley.edu`.

[43] Building Seismic Safety Council. *Recommended Seismic Provisions for New Buildings and Other Structures, Volume I: PART 1 Provisions, PART 2 Commentary. FEMA P-2082-1.* Washington DC, 2020.

[44] *Seismic Design Criteria for Structures, Systems, and Components in Nuclear Facilities*. American Society of Civil Engineers, January 2021. doi: 10.1061/9780784415405.

[45] C. Zhao, N. Yu, Y. Oz, J. Wang, and Y. L. Mo. Seismic fragility analysis of nuclear power plant structure under far-field ground motions. *Engineering Structures*, 219:110890, 2020. doi: 10.1016/j.engstruct.2020.110890.

[46] Duy-Duan Nguyen, Bidhek Thusa, Hyosang Park, Md Samdani Azad, and Tae-Hyung Lee. Efficiency of various structural modeling schemes on evaluating seismic performance and fragility of APR1400 containment building. *Nuclear Engineering and Technology*, 53(8):2696–2707, 2021. doi: 10.1016/j.net.2021.02.006.

[47] S. Jin, C. Zhai, J. Liu, D. Jiang, D. Wang, S. Wang, and Y. Zhou. Seismic fragility analysis of nuclear containment structure using bayesian logistic regression model. *Soil Dynamics and Earthquake Engineering*, 178:108435, 2024. doi: 10.1016/j.soildyn.2023.108435.

[48] Y.-G. Zhao, M.-J. Qin, Z.-H. Lu, and L.-W. Zhang. Seismic fragility analysis of nuclear power plants considering structural parameter uncertainty. *Reliability Engineering & System Safety*, 216:107970, 2021. doi: 10.1016/j.ress.2021.107970.

[49] J. P. Petti, B. W. Spencer, and H. L. Graves. Risk-informed assessment of degraded containment vessels. *Nuclear Engineering and Design*, 238(8):2038–2047, August 2008. doi: 10.1016/j.nucengdes.2007.10.025.

[50] C. Adam, D. Kampenhuber, and L. F. Ibarra. Optimal intensity measure based on spectral acceleration for p-delta vulnerable deteriorating frame structures in the collapse limit state. *Bulletin of Earthquake Engineering*, 15(10): 4349–4373, March 2017. doi: 10.1007/s10518-017-0129-3.

[51] R. Uribe, S. Sattar, M. S. Speicher, and L. Ibarra. Effect of common u.s. ground motion selection methods on the structural response of steel moment frame buildings. *Earthquake Spectra*, 35(4):1611–1635, 2019. doi: 10.1193/122917EQS268M.

[52] J. W. Baker. Efficient analytical fragility function fitting using dynamic structural analysis. *Earthquake Spectra*, 31(1):579–599, 2015. doi: 10.1193/021113EQS025M.